Supplemental Material: High-order harmonic generation in graphene: nonlinear coupling of intra and interband transitions

Shunsuke A. Sato,[1,2,*] Hideki Hirori,[3] Yasuyuki Sanari,[3] Yoshihiko Kanemitsu,[3] and Angel Rubio[2,4]

[1] *Center for Computational Sciences, University of Tsukuba, Tsukuba 305-8577, Japan*
[2] *Max Planck Institute for the Structure and Dynamics of Matter, Luruper Chaussee 149, 22761 Hamburg, Germany*
[3] *Institute for Chemical Research, Kyoto University, Uji, Kyoto 611-0011, Japan*
[4] *Center for Computational Quantum Physics (CCQ), Flatiron Institute, 162 Fifth Avenue, New York, NY 10010, USA*

I. EQUATION OF MOTION AND RELAXATION OPERATOR

Here, we describe the details of our theoretical modeling of electron dynamics in graphene under laser fields. The model has been introduced in the previous works [1, 2]. The electron dynamics is described by the following quantum master equation for the one-body electron density matrix,

$$\frac{d}{dt}\rho_{\boldsymbol{k}}(t) = \frac{1}{i\hbar}\left[H_{\boldsymbol{k}+\boldsymbol{A}(t)}\right] + \hat{D}\left[\rho_{\boldsymbol{k}}(t)\right], \tag{1}$$

where $H_{\boldsymbol{k}+\boldsymbol{A}(t)}$ is the time-dependent Hamiltonian and $\hat{D}\left[\rho_{\boldsymbol{k}}(t)\right]$ is a relaxation operator. In this work, we consider the following 2-by-2 Hamiltonian matrix

$$H_{\boldsymbol{k}+\boldsymbol{A}(t)} = v_F\tau_z\sigma_x\left[k_x + A_x(t)\right] + v_F\sigma_y\left[k_y + A_y(t)\right] + \frac{\Delta}{2}\sigma_z, \tag{2}$$

where σ_j are the Pauli matrices.

For the relaxation operator, we employ a simple relaxation time approximation [3] in the instantaneous eigenbasis expression [4, 5]. For this purpose, we first introduce instantaneous eigenstates of the Hamiltonian $H_{\boldsymbol{k}+\boldsymbol{A}(t)}$

$$H_{\boldsymbol{k}+\boldsymbol{A}(t)}\left|u_{b,\boldsymbol{k}+\boldsymbol{A}(t)}\right\rangle = \epsilon_{b,\boldsymbol{k}+\boldsymbol{A}(t)}\left|u_{b,\boldsymbol{k}+\boldsymbol{A}(t)}\right\rangle, \tag{3}$$

where b is a band index, $\left|u_{b,\boldsymbol{k}+\boldsymbol{A}(t)}\right\rangle$ are instantaneous eigenstates, and $\epsilon_{b,\boldsymbol{k}+\boldsymbol{A}(t)}$ are the corresponding single-particle energies. Note that, since we consider the 2-by-2 Hamiltonian, we have only two bands: one is the valence band ($b = v$), and the other is the conduction band ($b = c$). One can further introduce a unitary matrix $U_{\boldsymbol{k}+\boldsymbol{A}(t)}$ as $U_{\boldsymbol{k}+\boldsymbol{A}(t)} = \left(\left|u_{v,\boldsymbol{k}+\boldsymbol{A}(t)}\right\rangle, \left|u_{c,\boldsymbol{k}+\boldsymbol{A}(t)}\right\rangle\right)$. The introduced unitary matrix diagonalizes the Hamiltonian as

$$U^\dagger_{\boldsymbol{k}+\boldsymbol{A}(t)}H_{\boldsymbol{k}+\boldsymbol{A}(t)}U_{\boldsymbol{k}+\boldsymbol{A}(t)} = \begin{pmatrix} \epsilon_{v,\boldsymbol{k}+\boldsymbol{A}(t)} & 0 \\ 0 & \epsilon_{c,\boldsymbol{k}+\boldsymbol{A}(t)} \end{pmatrix}. \tag{4}$$

Based on the unitary matrix, we further introduce the one-body density matrix in the instantaneous eigenbasis representation as

$$\tilde{\rho}_{\boldsymbol{k}}(t) = \begin{pmatrix} \rho_{vv,\boldsymbol{k}}(t) & \rho_{vc,\boldsymbol{k}}(t) \\ \rho_{cv,\boldsymbol{k}}(t) & \rho_{cc,\boldsymbol{k}}(t) \end{pmatrix} = U^\dagger_{\boldsymbol{k}+\boldsymbol{A}(t)}\rho_{\boldsymbol{k}}(t)U_{\boldsymbol{k}+\boldsymbol{A}(t)}. \tag{5}$$

With the instantaneous eigenbasis representation, we consider the relaxation of the density matrix by introducing two kinds of relaxation: One is the longitudinal relaxation, which is the relaxation of the diagonal elements of the density matrix, while the other is the transverse relaxation, which is the relaxation of the off-diagonal elements. To realize such relaxation in a practical implementation, we introduce the relaxation operator as

$$\hat{D}\left[\rho_{\boldsymbol{k}}(t)\right] = -U_{\boldsymbol{k}}(t)\begin{pmatrix} \frac{\rho_{vv,\boldsymbol{k}}(t)-\rho^F_{v,\boldsymbol{k}+\boldsymbol{A}(t)}}{T_1} & \frac{\rho_{vc,\boldsymbol{k}}(t)}{T_2} \\ \frac{\rho_{cv,\boldsymbol{k}}(t)}{T_2} & \frac{\rho_{cc,\boldsymbol{k}}(t)-\rho^F_{c,\boldsymbol{k}+\boldsymbol{A}(t)}}{T_1} \end{pmatrix}U^\dagger_{\boldsymbol{k}}(t), \tag{6}$$

* ssato@ccs.tsukuba.ac.jp

where T_1 and T_2 are the time-constants for the longitudinal and transverse relaxations, respectively. In this work, as a target state of the relaxation, we employ the Fermi-Dirac distribution

$$\rho^F_{b,\boldsymbol{k}} = \frac{1}{e^{(\epsilon_{b,\boldsymbol{k}}-\mu)/k_B T_e}+1}, \tag{7}$$

where μ is the chemical potential, T_e is the electron temperature. In this work, we fix the electron temperature T_e to 80 K.

II. FOCAL SPOT AVERAGE

In realistic experimental configurations, the high-order harmonic generation occurs not only at the center of a beam-spot but also on the whole focal area. Thus, the generated high-order harmonics from a wide region of the focal area can be detected. To take into account the macroscopic focal-spot average effect of HHG, we employ the intensity average procedure according to Ref. [6].

Here, we assume the field strength of laser electric fields has the following Gaussian profile on the sample surface

$$E(x,y) = E_0 \exp\left[-\frac{1}{\sigma^2}\left(x^2+y^2\right)\right], \tag{8}$$

where (x,y) are the coordinates on the surface, E_0 is the peak field strength, and σ is the beam waist. We further assume that the beam waist is sufficiently large, and the induced current depends only on the local field strength as $\boldsymbol{J}[E(x,y)](t)$. Based on these assumptions, the average current within the beam spot can be evaluated as

$$\boldsymbol{J}^{ave}(t) = \frac{1}{\pi\sigma^2}\int dxdy \boldsymbol{J}[E(x,y)] = \int_0^1 d\alpha \frac{1}{\alpha}\boldsymbol{J}[\alpha E_0](t). \tag{9}$$

Hence the total current on the sample can be evaluated as the intensity average of the induced current. In this work, we repeatedly perform the simulation by changing the laser field strength $E_0 = \sqrt{E_{0,x}^2 + E_{0,y}^2}$ with fixed ratio of $E_{0,x}$ and $E_{0,y}$. Then, we compute the averaged current on the sample $\boldsymbol{J}^{ave}(t)$ with Eq. (9).

III. DECOMPOSITION OF INTRABAND AND INTERBAND TRANSITIONS

In this work, we define intraband and interband transitions based on the instantaneous eigenbasis representation [4, 5]. To define the intraband and interband transitions, we first consider the equation of motion of the reduced density matrix in the instantaneous eigenbasis representation as

$$\begin{aligned}\frac{d}{dt}\tilde{\rho}_{\boldsymbol{k}}(t) &= \frac{d}{dt}U^\dagger_{\boldsymbol{k}+\boldsymbol{A}(t)}\rho_{\boldsymbol{k}}(t)U_{\boldsymbol{k}+\boldsymbol{A}(t)} = \frac{dU^\dagger_{\boldsymbol{k}+\boldsymbol{A}(t)}}{dt}\rho_{\boldsymbol{k}}(t)U_{\boldsymbol{k}+\boldsymbol{A}(t)} + U^\dagger_{\boldsymbol{k}+\boldsymbol{A}(t)}\frac{d\rho_{\boldsymbol{k}}(t)}{dt}U_{\boldsymbol{k}+\boldsymbol{A}(t)} + U^\dagger_{\boldsymbol{k}+\boldsymbol{A}(t)}\rho_{\boldsymbol{k}}(t)\frac{dU_{\boldsymbol{k}+\boldsymbol{A}(t)}}{dt} \\ &= \frac{1}{i\hbar}\left[\tilde{H}_{\boldsymbol{k}+\boldsymbol{A}(t)},\tilde{\rho}_{\boldsymbol{k}}(t)\right] - \begin{pmatrix} \frac{\rho_{vv,\boldsymbol{k}}(t)-\rho^F_{v,\boldsymbol{k}+\boldsymbol{A}(t)}}{T_1} & \frac{\rho_{vc,\boldsymbol{k}}(t)}{T_2} \\ \frac{\rho_{cv,\boldsymbol{k}}(t)}{T_2} & \frac{\rho_{cc,\boldsymbol{k}}(t)-\rho^F_{c,\boldsymbol{k}+\boldsymbol{A}(t)}}{T_1}\end{pmatrix},\end{aligned} \tag{10}$$

where the effective Hamiltonian $\tilde{H}_{\boldsymbol{k}+\boldsymbol{A}(t)}$ in the instantaneous eigenbasis representation is given by

$$\tilde{H}_{\boldsymbol{k}+\boldsymbol{A}(t)} = \begin{pmatrix}\epsilon_{v,\boldsymbol{k}+\boldsymbol{A}(t)} & 0 \\ 0 & \epsilon_{c,\boldsymbol{k}+\boldsymbol{A}(t)}\end{pmatrix} + i\hbar\begin{pmatrix} \left\langle\frac{\partial u_{v,\boldsymbol{k}+\boldsymbol{A}(t)}}{\partial\boldsymbol{k}}\middle|u_{v,\boldsymbol{k}+\boldsymbol{A}(t)}\right\rangle\cdot\dot{\boldsymbol{A}}(t), & \left\langle\frac{\partial u_{v,\boldsymbol{k}+\boldsymbol{A}(t)}}{\partial\boldsymbol{k}}\middle|u_{c,\boldsymbol{k}+\boldsymbol{A}(t)}\right\rangle\cdot\dot{\boldsymbol{A}}(t) \\ \left\langle\frac{\partial u_{c,\boldsymbol{k}+\boldsymbol{A}(t)}}{\partial\boldsymbol{k}}\middle|u_{v,\boldsymbol{k}+\boldsymbol{A}(t)}\right\rangle\cdot\dot{\boldsymbol{A}}(t), & \left\langle\frac{\partial u_{c,\boldsymbol{k}+\boldsymbol{A}(t)}}{\partial\boldsymbol{k}}\middle|u_{c,\boldsymbol{k}+\boldsymbol{A}(t)}\right\rangle\cdot\dot{\boldsymbol{A}}(t)\end{pmatrix}. \tag{11}$$

To naturally distinguish the intraband and interband transitions, we rewrite the Hamiltonian with the new gauge fields, $\boldsymbol{A}_{tra}$ and $\boldsymbol{A}_{ter}(t)$ as

$$\tilde{H}^{\mathrm{tra-ter}}_{\boldsymbol{k}+\boldsymbol{A}(t)} = \begin{pmatrix}\epsilon_{v,\boldsymbol{k}+\boldsymbol{A}_{tra}(t)} & 0 \\ 0 & \epsilon_{c,\boldsymbol{k}+\boldsymbol{A}_{tra}(t)}\end{pmatrix} + i\hbar\begin{pmatrix} \left\langle\frac{\partial u_{v,\boldsymbol{k}+\boldsymbol{A}_{tra}(t)}}{\partial\boldsymbol{k}}\middle|u_{v,\boldsymbol{k}+\boldsymbol{A}_{tra}(t)}\right\rangle\cdot\dot{\boldsymbol{A}}_{tra}(t), & \left\langle\frac{\partial u_{v,\boldsymbol{k}+\boldsymbol{A}_{tra}(t)}}{\partial\boldsymbol{k}}\middle|u_{c,\boldsymbol{k}+\boldsymbol{A}_{tra}(t)}\right\rangle\cdot\dot{\boldsymbol{A}}_{ter}(t) \\ \left\langle\frac{\partial u_{c,\boldsymbol{k}+\boldsymbol{A}_{tra}(t)}}{\partial\boldsymbol{k}}\middle|u_{v,\boldsymbol{k}+\boldsymbol{A}_{tra}(t)}\right\rangle\cdot\dot{\boldsymbol{A}}_{ter}(t), & \left\langle\frac{\partial u_{c,\boldsymbol{k}+\boldsymbol{A}_{tra}(t)}}{\partial\boldsymbol{k}}\middle|u_{c,\boldsymbol{k}+\boldsymbol{A}_{tra}(t)}\right\rangle\cdot\dot{\boldsymbol{A}}_{tra}(t)\end{pmatrix}. \tag{12}$$

Note that, if $\boldsymbol{A}_{tra}(t) = \boldsymbol{A}_{ter}(t) = \boldsymbol{A}(t)$, the new Hamiltonian $\tilde{H}^{\mathrm{tra-ter}}_{\boldsymbol{k}+\boldsymbol{A}(t)}$ in Eq. (12) is identical to the original Hamiltonian $\tilde{H}_{\boldsymbol{k}+\boldsymbol{A}(t)}$ in Eq. (11). If $\boldsymbol{A}_{tra}(t) = \boldsymbol{A}(t)$ and $\boldsymbol{A}_{ter}(t) = 0$, the system is adiabatically evolved within the same

band. Hence the transitions induced by $\boldsymbol{A}_{tra}(t)$ is nothing but the intraband transitions. On the other hand, if $\boldsymbol{A}_{tra}(t) = 0$ and $\boldsymbol{A}_{ter}(t) = \boldsymbol{A}(t)$, the system shows only a transition among different bands without the motion in the k-space. Hence the transitions induced by $\boldsymbol{A}_{ter}(t)$ is nothing but the interband transitions. Note that these definitions of the intraband and interband transitions with the reduced density matrix are equivalent to those defined with the Houston expansion in the wavefunction theory [7].

Based on the electron dynamics simulations with the effective Hamiltonian $\tilde{H}^{\mathrm{tra-ter}}_{\boldsymbol{k}+\boldsymbol{A}(t)}$, one can elucidate impacts of intraband and interband transitions. For example, by setting $\boldsymbol{A}_{tra}(t)$ to $\boldsymbol{A}(t)$ and $\boldsymbol{A}_{ter}(t)$ to zero, one can study the electron dynamics induced solely by the intraband transitions. Likewise, by setting $\boldsymbol{A}_{tra}(t)$ to zero and $\boldsymbol{A}_{ter}(t)$ to $\boldsymbol{A}(t)$, one can study the electron dynamics induced solely by the interband transitions. Applying this approach to the HHG in graphene, we evaluated the high-order harmonic intensity induced solely by intraband or interband transitions. The results are shown in Fig. 2 (e) in the main text.

To investigate detailed roles of nonlinear coupling among intraband and interband transitions, we introduce a decomposition of the current $\boldsymbol{J}(t, E_{0,x}, E_{0,y})$ into each nonlinear coupling component. In the above analysis, we introduced the two gauge fields, $\boldsymbol{A}_{tra}(t)$ and $\boldsymbol{A}_{ter}(t)$, to distinguish the intraband and interband transitions. Furthermore, each gauge field vector consists of two directional components. Hence, the induced current is a function of the field strength of each component of each gauge field as $\boldsymbol{J}^{\mathrm{tra-ter}}(t, E_{0,x,tra}, E_{0,x,ter}, E_{0,y,tra}, E_{0,y,ter})$. In the main text, we introduced the following four labels for each kind of transitions. τ_a: the intraband transitions induced by the x-component of fields. τ_b: the interband transitions induced by the x-component of fields. τ_c: the intraband transitions induced by the y-component of fields. τ_d: the interband transitions induced by the y-component of fields. With this notation, we first define four kinds of current as follows:

$$\boldsymbol{J}_{\tau_a}(t) = \boldsymbol{J}^{\mathrm{tra-ter}}(t, E_{0,x,tra}, 0, 0, 0), \tag{13}$$

$$\boldsymbol{J}_{\tau_b}(t) = \boldsymbol{J}^{\mathrm{tra-ter}}(t, 0, E_{0,x,ter}, 0, 0), \tag{14}$$

$$\boldsymbol{J}_{\tau_c}(t) = \boldsymbol{J}^{\mathrm{tra-ter}}(t, 0, 0, E_{0,y,tra}, 0), \tag{15}$$

$$\boldsymbol{J}_{\tau_d}(t) = \boldsymbol{J}^{\mathrm{tra-ter}}(t, 0, 0, 0, E_{0,y,ter}). \tag{16}$$

Each of them corresponds to the current induced solely by a single-directional component of each transition: $\boldsymbol{J}_{\tau_a}(t)$ is induced solely by the x-component of intraband transitions, and $\boldsymbol{J}_{\tau_b}(t)$ is induced solely by the x-component of inter transitions. Likewise, $\boldsymbol{J}_{\tau_c}(t)$ is induced solely by the y-component of intraband transitions, and $\boldsymbol{J}_{\tau_d}(t)$ is induced solely by the y-component of interband transitions.

Then, we define the current induced by nonlinear coupling of two of four components as

$$\boldsymbol{J}_{\tau_a,\tau_b}(t) = \boldsymbol{J}^{\mathrm{tra-ter}}(t, E_{0,x,tra}, E_{0,x,ter}, 0, 0,) - \boldsymbol{J}_{\tau_a}(t) - \boldsymbol{J}_{\tau_b}(t) \tag{17}$$

$$\boldsymbol{J}_{\tau_a,\tau_c}(t) = \boldsymbol{J}^{\mathrm{tra-ter}}(t, E_{0,x,tra}, 0, E_{0,y,tra}, 0) - \boldsymbol{J}_{\tau_a}(t) - \boldsymbol{J}_{\tau_c}(t) \tag{18}$$

$$\boldsymbol{J}_{\tau_a,\tau_d}(t) = \boldsymbol{J}^{\mathrm{tra-ter}}(t, E_{0,x,tra}, 0, 0, E_{0,y,ter}) - \boldsymbol{J}_{\tau_a}(t) - \boldsymbol{J}_{\tau_d}(t) \tag{19}$$

$$\boldsymbol{J}_{\tau_b,\tau_c}(t) = \boldsymbol{J}^{\mathrm{tra-ter}}(t, 0, E_{0,x,ter}, E_{0,y,tra}, 0) - \boldsymbol{J}_{\tau_b}(t) - \boldsymbol{J}_{\tau_c}(t) \tag{20}$$

$$\boldsymbol{J}_{\tau_b,\tau_d}(t) = \boldsymbol{J}^{\mathrm{tra-ter}}(t, 0, E_{0,x,ter}, 0, E_{0,y,ter}) - \boldsymbol{J}_{\tau_b}(t) - \boldsymbol{J}_{\tau_d}(t) \tag{21}$$

$$\boldsymbol{J}_{\tau_c,\tau_d}(t) = \boldsymbol{J}^{\mathrm{tra-ter}}(t, 0, 0, E_{0,y,tra}, E_{0,y,ter}) - \boldsymbol{J}_{\tau_c}(t) - \boldsymbol{J}_{\tau_d}(t). \tag{22}$$

Here, $\boldsymbol{J}_{\tau_a,\tau_b}(t)$ is induced by the nonlinear coupling of the x-components of the intraband and interband transitions, $\boldsymbol{J}_{\tau_a,\tau_c}(t)$ is induced by the nonlinear coupling of the x- and y-components of the intraband transitions, $\boldsymbol{J}_{\tau_a,\tau_d}(t)$ is induced by the nonlinear coupling of the x-component of the intraband and the y-component of the interband transitions, $\boldsymbol{J}_{\tau_b,\tau_c}(t)$ is induced by the nonlinear coupling of the x-component of the interband and the y-component of the intraband transitions, $\boldsymbol{J}_{\tau_b,\tau_d}(t)$ is induced by the nonlinear coupling of the x- and y-components of the interband transitions, and $\boldsymbol{J}_{\tau_c,\tau_d}(t)$ is induced by the nonlinear coupling of the y-components of the intraband and intraband transitions.

In the same way, we define the current induced by nonlinear coupling among three of four field components as

$$\begin{aligned}\boldsymbol{J}_{\tau_a,\tau_b,\tau_c}(t) = \boldsymbol{J}^{\mathrm{tra-ter}}(t, E_{0,x,tra}, E_{0,x,ter}, E_{0,y,tra}, 0) - \boldsymbol{J}_{\tau_a,\tau_b}(t) - \boldsymbol{J}_{\tau_a,\tau_c}(t) - \boldsymbol{J}_{\tau_b,\tau_c}(t) \\ -\boldsymbol{J}_{\tau_a}(t) - \boldsymbol{J}_{\tau_b}(t) - \boldsymbol{J}_{\tau_c}(t)\end{aligned} \tag{23}$$

$$\begin{aligned}\boldsymbol{J}_{\tau_a,\tau_b,\tau_d}(t) = \boldsymbol{J}^{\mathrm{tra-ter}}(t, E_{0,x,tra}, E_{0,x,ter}, 0, E_{0,y,ter}) - \boldsymbol{J}_{\tau_a,\tau_b}(t) - \boldsymbol{J}_{\tau_a,\tau_d}(t) - \boldsymbol{J}_{\tau_b,\tau_d}(t) \\ -\boldsymbol{J}_{\tau_a}(t) - \boldsymbol{J}_{\tau_b}(t) - \boldsymbol{J}_{\tau_d}(t)\end{aligned} \tag{24}$$

$$\begin{aligned}\boldsymbol{J}_{\tau_a,\tau_c,\tau_d}(t) = \boldsymbol{J}^{\mathrm{tra-ter}}(t, E_{0,x,tra}, 0, E_{0,y,tra}, E_{0,y,ter}) - \boldsymbol{J}_{\tau_a,\tau_c}(t) - \boldsymbol{J}_{\tau_a,\tau_d}(t) - \boldsymbol{J}_{\tau_c,\tau_d}(t) \\ -\boldsymbol{J}_{\tau_a}(t) - \boldsymbol{J}_{\tau_c}(t) - \boldsymbol{J}_{\tau_d}(t)\end{aligned} \tag{25}$$

$$\begin{aligned}\boldsymbol{J}_{\tau_b,\tau_c,\tau_d}(t) = \boldsymbol{J}^{\mathrm{tra-ter}}(t, 0, E_{0,x,ter}, E_{0,y,tra}, E_{0,y,ter}) - \boldsymbol{J}_{\tau_b,\tau_c}(t) - \boldsymbol{J}_{\tau_b,\tau_d}(t) - \boldsymbol{J}_{\tau_c,\tau_d}(t) \\ -\boldsymbol{J}_{\tau_b}(t) - \boldsymbol{J}_{\tau_c}(t) - \boldsymbol{J}_{\tau_d}(t).\end{aligned} \tag{26}$$

Finally, we define the current induced by nonlinear coupling of all of the field components as

$$\begin{aligned}\boldsymbol{J}_{\tau_a,\tau_b,\tau_c,\tau_d}(t) = \boldsymbol{J}^{\mathrm{tra-ter}}(t, E_{0,x,tra}, E_{0,x,ter}, E_{0,y,tra}, E_{0,y,ter}) - \boldsymbol{J}_{\tau_a,\tau_b,\tau_c}(t) - \boldsymbol{J}_{\tau_a,\tau_b,\tau_d}(t) - \boldsymbol{J}_{\tau_a,\tau_c,\tau_d}(t) - \boldsymbol{J}_{\tau_b,\tau_c,\tau_d}(t) \\ - \boldsymbol{J}_{\tau_a,\tau_b}(t) - \boldsymbol{J}_{\tau_a,\tau_c}(t) - \boldsymbol{J}_{\tau_a,\tau_d}(t) - \boldsymbol{J}_{\tau_b,\tau_c}(t) - \boldsymbol{J}_{\tau_b,\tau_d}(t) - \boldsymbol{J}_{\tau_c,\tau_d}(t) \\ - \boldsymbol{J}_{\tau_a}(t) - \boldsymbol{J}_{\tau_b}(t) - \boldsymbol{J}_{\tau_c}(t) - \boldsymbol{J}_{\tau_d}(t). \end{aligned} \tag{27}$$

By construction of the decomposed current in Eqs. (13-27), the total current $\boldsymbol{J}(t, E_{0,x}, E_{0,y})$ is fully reconstructed as

$$\begin{aligned}\boldsymbol{J}(t, E_{0,x}, E_{0,y}) = \boldsymbol{J}_{\tau_a}(t) + \boldsymbol{J}_{\tau_b}(t)\boldsymbol{J}_{\tau_c}(t) + \boldsymbol{J}_{\tau_d}(t) \\ + \boldsymbol{J}_{\tau_a,\tau_b}(t) + \boldsymbol{J}_{\tau_a,\tau_c}(t) + \boldsymbol{J}_{\tau_a,\tau_d}(t) + \boldsymbol{J}_{\tau_b,\tau_c}(t) + \boldsymbol{J}_{\tau_b,\tau_d}(t) + \boldsymbol{J}_{\tau_c,\tau_d}(t) \\ + \boldsymbol{J}_{\tau_a,\tau_b,\tau_c}(t) + \boldsymbol{J}_{\tau_a,\tau_b,\tau_d}(t) + \boldsymbol{J}_{\tau_a,\tau_c,\tau_d}(t) + \boldsymbol{J}_{\tau_b,\tau_c,\tau_d}(t) \\ + \boldsymbol{J}_{\tau_a,\tau_b,\tau_c,\tau_d}(t). \end{aligned} \tag{28}$$

Note that the decomposition of the current in Eq. (28) is conceptually similar to a decomposition proposed in Ref. [8] since both decompositions are based on the intraband and interband transitions. In the previous decomposition, the current is decomposed at each nonlinear order. In contrast, the above decomposition does not rely on the perturbative expansion but directly decomposes the current, including all order of the nonlinear contributions at once. Hence, the decomposition of Eq. (28) is suitable for the analysis of the non-perturbative nonlinear phenomena such as HHG in solids.

We evaluated the harmonic intensity with each decomposed current. Figures S1-S3 show the 7th-order harmonic intensity I_y^{7th} as a function of ellipticity for various decomposed current. Here, we employed the same conditions as those of Fig. 2 (f) of the main text. In Fig. S1, the results of the current induced sorely by a single transition, $\boldsymbol{J}_\tau$, are shown. In Fig. S2, the results of the current induced by the nonlinear coupling between two of four kinds of transitions, $\boldsymbol{J}_{\tau\sigma}$, are shown. In Fig. S3, the results of the current induced by the nonlinear coupling among three of four transitions, $\boldsymbol{J}_{\tau\sigma\delta}$, and among all of four transitions, $\boldsymbol{J}_{\tau_a,\tau_b,\tau_c,\tau_d}(t)$, are shown. In these figures, the result of the full transitions is also shown as the black-solid line.

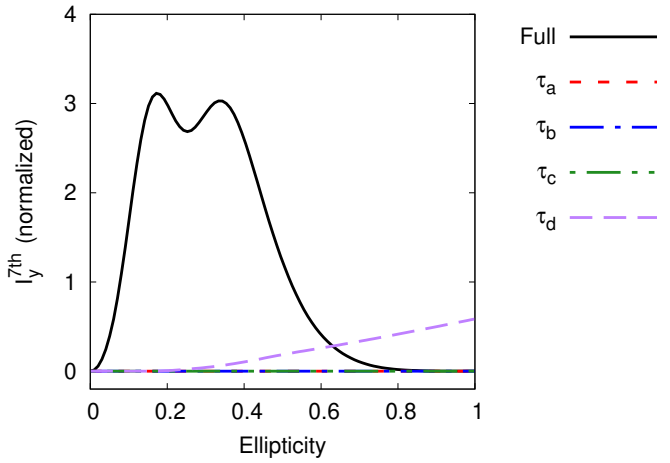

FIG. S1: The 7th-order HHG from graphene under elliptically polarized light. Here, the contributions from each single transition $\boldsymbol{J}_\tau$ in Eqs. (13-16) are shown.

IV. FIELD STRENGTH DEPENDENCE AND OTHER ORDER HARMONICS

In the main text, we studied the 7th-order harmonics with the peak field strength $\sqrt{E_{0,x}^2 + E_{0,y}^2}$ of 6.5 MV/cm. As seen from Fig. 1 (a) in the main text, the corresponding simulation fairly reproduces the experimental results [9]. Note that the estimated experimental field strength is about 20 MV/cm, and our field strength of 6.5 MV/cm is consistent with the experimental field strength. Hence, our simulations are performed with realistic condition. Although the previous theoretical simulation [9] also reproduced the experimental results fairly well, the relation of the experimental and simulation parameters is unclear.

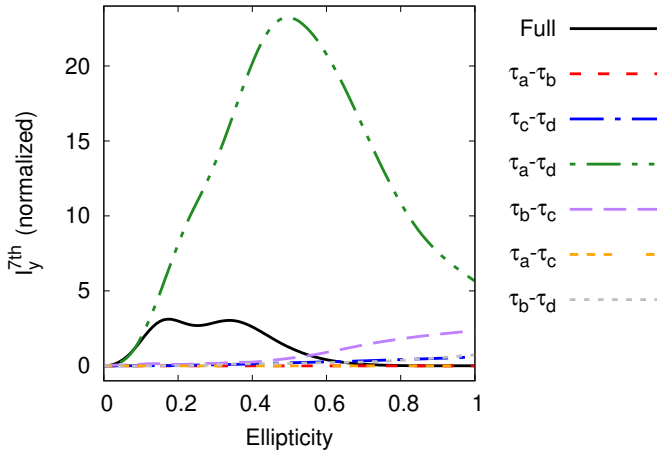

FIG. S2: The 7th-order HHG from graphene under elliptically polarized light. Here, the contributions from nonlinear coupling of two of four transitions $\boldsymbol{J}_{\tau\sigma}$ in Eqs. (17-22) are shown.

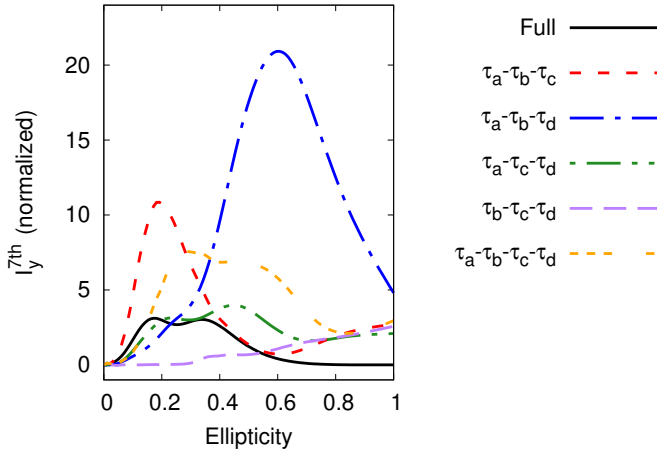

FIG. S3: The 7th-order HHG from graphene under elliptically polarized light. Here, the contributions from nonlinear coupling of three of four transitions $\boldsymbol{J}_{\tau\sigma\delta}$ in Eqs. (23-26) are shown. The contribution from the nonlinear coupling of all of the transitions $\boldsymbol{J}_{\tau_a,\tau_b,\tau_c,\tau_d}(t)$ in Eq. (27) is also shown.

To confirm the robustness of the enhancement of the HHG in graphene by elliptically polarized light, we performed the simulation with higher field strength $\sqrt{E_{0,x}^2 + E_{0,y}^2}$ of 21 MV/cm. Figure S4 shows the computed 7th-order harmonic intensity as a function of ellipticity. In the simulation the same conditions were employed as Fig. 1 (a) in the main text exept the field strength. As seen from the figure, the clear enhancement of the harmonic intensity by elliptically polarized light can be confirmed. Hence, the enhancement is robust against to the field strength change.

Next, we investigate the ellipticity dependence of the HHG in other orders. Figure S5 shows the harmonic intensities for different harmonic orders as functions of ellipticity. In this analysis, we employed the same conditions as Fig. 1 (a) in the main text. Therefore, the result of the 7th harmonics in Figure S5 (b) is identical to that of Fig. 1 (a). As seen from Figs S5 (a)-(c), the elliptically polarized light enhances the harmonic intensity at the 5th, 7th, and 9th order. Thus, we can confirm that the enhancement of the HHG in graphene by elliptically polarized light is not only for the 7th-order harmonics but rather general phenomena.

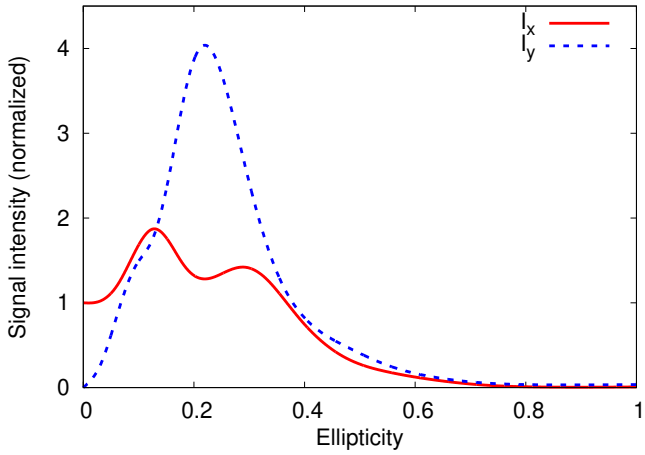

FIG. S4: The 7th-order harmonic intensity from graphene as a function of ellipticity.

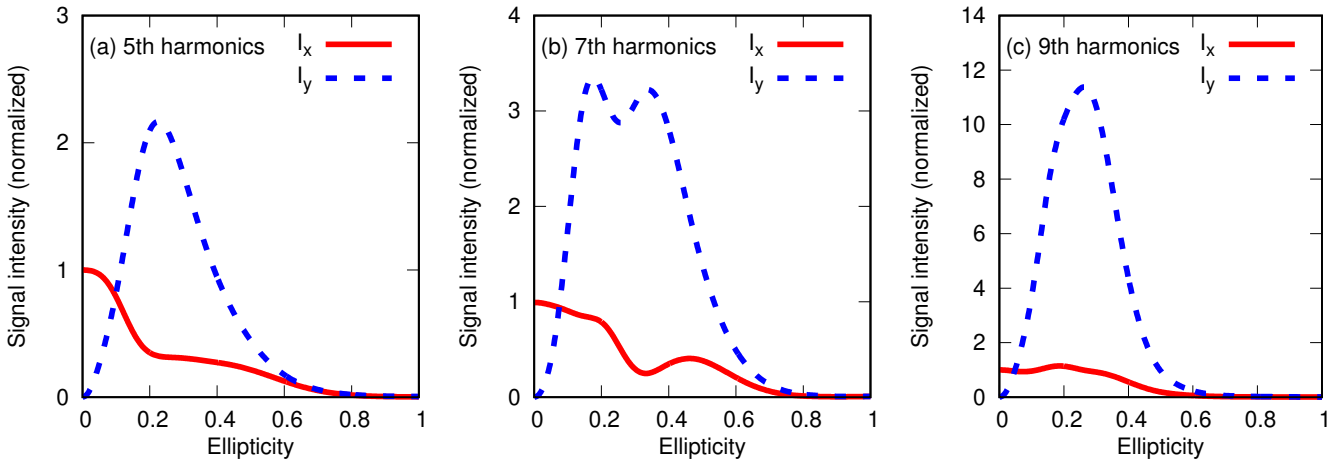

FIG. S5: Ellipticity dependence of the harmonic intensity. The results for different harmonic orders are shown: (a) 5th, (b) 7th, and (c) 9th order harmonics.

[1] S. A. Sato, J. W. McIver, M. Nuske, P. Tang, G. Jotzu, B. Schulte, H. Hübener, U. De Giovannini, L. Mathey, M. A. Sentef, A. Cavalleri, and A. Rubio, Phys. Rev. B **99**, 214302 (2019).
[2] S. A. Sato, P. Tang, M. A. Sentef, U. D. Giovannini, H. Hübener, and A. Rubio, New Journal of Physics **21**, 093005 (2019).
[3] T. Meier, G. von Plessen, P. Thomas, and S. W. Koch, Phys. Rev. Lett. **73**, 902 (1994).
[4] W. V. Houston, Phys. Rev. **57**, 184 (1940).
[5] J. B. Krieger and G. J. Iafrate, Phys. Rev. B **33**, 5494 (1986).
[6] I. Floss, C. Lemell, G. Wachter, V. Smejkal, S. A. Sato, X.-M. Tong, K. Yabana, and J. Burgdörfer, Phys. Rev. A **97**, 011401 (2018).
[7] S. A. Sato, M. Lucchini, M. Volkov, F. Schlaepfer, L. Gallmann, U. Keller, and A. Rubio, Phys. Rev. B **98**, 035202 (2018).
[8] C. Aversa and J. E. Sipe, Phys. Rev. B **52**, 14636 (1995).
[9] N. Yoshikawa, T. Tamaya, and K. Tanaka, Science **356**, 736 (2017).